Biosensors and Bioelectronics 126 (2019) 44–50

Contents lists available at ScienceDirect

Biosensors and Bioelectronics

journal homepage: www.elsevier.com/locate/bios

High performance UV photodetectors using Nd^{3+} and Er^{3+} single- and co-doped DNA thin films

Srivithya Vellampatti[a,1], Maddaka Reddeppa[b,1], Sreekantha Reddy Dugasani[a,1], Sekhar Babu Mitta[a], Bramaramba Gnapareddy[a], Moon-Deock Kim[b,*], Sung Ha Park[a,*]

[a] Sungkyunkwan Advanced Institute of Nanotechnology (SAINT) and Department of Physics, Sungkyunkwan University, Suwon 16419, Republic of Korea
[b] Department of Physics, Chungnam National University, Daejeon 34134, Republic of Korea

ARTICLE INFO

Keywords:
DNA
Thin film
Neodymium and erbium ions
Doping
Photodetector

ABSTRACT

Even though lanthanide ion (Ln^{3+})-doped DNA nanostructures have been utilized in various applications, they are rarely employed for photovoltage generating devices because of difficulties in designing DNA-based devices that generate voltages under light illumination. Here, we constructed DNA lattices made of synthetic strands and DNA thin films extracted from salmon (SDNA) with single-doping of Nd^{3+} or Er^{3+} and co-doping of Nd^{3+}/Er^{3+} for high performance UV detection. The topological change of the DNA double-crossover (DX) lattices during the course of annealing was estimated from atomic force microscope (AFM) images to find the optimum concentration of Ln^{3+} ($[Ln^{3+}]_O$). No topological disturbance in DNA DX lattices were observed up to $[Ln^{3+}]_O$, and significant enhancement in the physical properties was obtained at $[Ln^{3+}]_O$. The interactions between Ln^{3+} and SDNA were examined using spectroscopic methods of UV–visible, Raman, and X-ray photoelectron spectroscopy (XPS). Current and photovoltage measurements for Ln^{3+}-doped SDNA thin films under UV illumination with varying power intensities were conducted. Under UV illumination, the photocurrent and photovoltage of Ln^{3+}-doped SDNA thin films increased with increasing applied external voltages and input power intensities, respectively. In addition, we observed considerable increases in photovoltage responses, *i.e.*, 5-fold increase for Nd^{3+}, 10-fold for Er^{3+}, and 13-fold for Nd^{3+}/Er^{3+}, compared to the pristine SDNA due to the additional charge carriers generated in Ln^{3+}-doped SDNA thin films. Device performance was measured in terms of photovoltage responsivity and retention characteristics. These phenomena indicate the high stability and substantial endurance characteristics of Ln^{3+}-doped SDNA thin films.

1. Introduction

DNA duplex is a macromolecule with a helical structure formed by alternating nucleotides that are bound through complementary base pairs *via* hydrogen bonding. DNA has gained popularity as a construction building block in the field of nanotechnology due to the self-assembly characteristic of base-pair recognition, molecular programmability through specific sequence design, and its relative stability compared to other biomolecules. DNA nanotechnology emerged in the beginning of the 1980s and has been developed to construct various dimensional structures with nanometer scale precision by sequence design (Seeman, 2003; Winfree et al., 1998; Nummelin et al., 2018). Furthermore, naturally available DNA (*e.g.*, extracted from salmon fish) has been used for various applications due to the easy manipulation, non-toxicity, water-solubility, mass production, and relatively low cost.

The incorporation of functional nanomaterials (such as metallic, semiconducting, magnetic, and dielectric nanoparticles, fluorescent dyes, carbon-based materials, proteins, and drug molecules as well as metal and rare earth ions) either in synthetic or natural DNA nanostructures has allowed us to create efficient working devices or sensors for use in physical, chemical, and biological applications (Vellampatti et al., 2015; Mitta et al., 2017; Rakitin et al., 2001; Pei et al., 2012; Halley et al., 2016; Vellampatti et al., 2018). DNA (served as a scaffold or template) hosts the functional nanomaterials to construct function-embedded DNA nanostructures with ease due to its unique geometry and negatively charged nature as well as its easy modification. Among the nanomaterials, ions in DNA nanostructures have significant advantages for construction of specific function-embedded devices or sensors due to the applicability of various types of ions having their own specific functions (which allow function tuning of the host

* Corresponding authors.
E-mail addresses: mdkim@cnu.ac.kr (M.-D. Kim), sunghapark@skku.edu (S.H. Park).
[1] These authors contribute equally to this work.

https://doi.org/10.1016/j.bios.2018.10.042
Received 7 August 2018; Received in revised form 16 October 2018; Accepted 22 October 2018
Available online 24 October 2018
0956-5663/

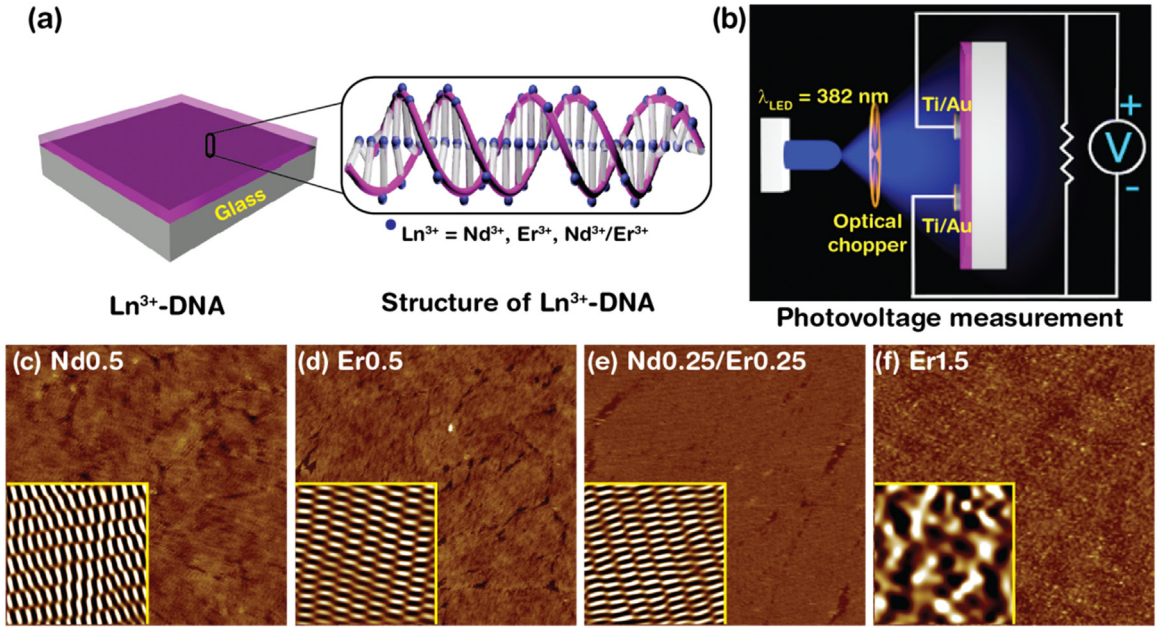

Fig. 1. Schematic representation of Ln^{3+}-doped DNA thin film, photovoltage measurement, and characteristic AFM images of Ln^{3+}-doped DNA double-crossover (DX) lattices. (a) Fabrication of the Ln^{3+}-doped DNA thin film on a given substrate and Ln^{3+} coordination in DNA. (b) Utilization of Ln^{3+}-doped DNA films for photo detection under UV illumination. (c-f) AFM images of DNA DX lattices having [Nd^{3+}], [Er^{3+}], [Nd^{3+}/Er^{3+}] (co-doped), and [Er^{3+}] of 0.5, 0.5, 0.25, and 1.5 mM, respectively labeled as Nd0.5, Er0.5, Nd0.25/Er0.25, and Er1.5. Insets in (c, d, e; the fast Fourier transform images) and (f) display the periodicities and aperiodicities of the DNA DX tiles, respectively. Scan sizes of the images and insets are 1 μm × 1 μm and 100 nm × 100 nm, respectively.

materials) and intrinsic geometrical atomic size (which has relatively less effect on the formation of the DNA duplexes compared to other functional nanomaterials) (Dugasani et al., 2015a, 2015b, 2015c).

Although they are used and developed in applications of various devices and sensors such as tunnel diodes (function-embedded DNA served as a tunnelling barrier), solar cells (as a blocking layer), thin-film transistors (as an active layer), electronic band gap devices (as a band gap reduction medium), hall transporters (as a charge carrier), magnetic devices (as a spin-aligner), α- and β-radiation detectors (as a sensing medium), and methanol volatile organic compound (VOC) sensors (as a sensing medium), function-embedded DNA nanostructures for photovoltage generation devices were seldom discussed because of difficulties in fabricating DNA samples that generate voltage under light illumination with enhanced sensitivity (Yoon et al., 2017; Lee et al., 2011; Jung et al., 2012; Dugasani et al., 2014a, 2014b; Dugasani et al., 2015a, 2015b, 2015c; Dugasani et al., 2013; Dugasani et al., 2014a, 2014b; Kim et al., 2015). Photodetectors are sensors of light with specific electromagnetic wavelengths. Photo detection in the UV range is considered to be an interesting research field due to its high sensitivity, stability, signal-to-noise ratio, and potential use in optoelectronic applications (Osinsky et al., 1997; Khokhra et al., 2017; Gong et al., 2009). Consequently, (i) construction of DNA nanostructures with specific functionalized materials that can sense UV light with high sensitivity and responsivity is very challenging and (ii) understanding the charge transport mechanism in function-embedded DNA nanostructures during UV illumination is demanding.

Here, we construct DNA double-crossover (DX) lattices made of sequence-designed synthetic DNA strands and naturally available salmon DNA (SDNA) thin films doped with single (*i.e.*, neodymium ion (Nd^{3+}), erbium ion (Er^{3+})), and co-doped lanthanide ions (Ln^{3+}) (*i.e.*, Nd^{3+} and Er^{3+} mixed). Rare earth Ln^{3+} (*i.e.*, Nd^{3+} and Er^{3+}) was chosen due to the unique optical and chemical properties of 4 f electrons (Dugasani et al., 2015a, 2015b, 2015c). Rare earth Ln^{3+} possesses high luminescence and photo stable characteristics, and is easily bound to DNA molecules without any modifications. Consequently, they can be used in waveguide optical devices, cryogenics applications, light-emitting diodes, and fiber optics (Reisfeld, 1987; Song et al., 2013). We successfully fabricated Ln^{3+}−doped DNA DX lattices and Ln^{3+}−doped SDNA thin films for high performance photo detection under UV illumination by optimizing the concentration of dopant [Ln^{3+}]. Optimum concentrations of the ions, $[Ln^{3+}]_O$ were obtained by analyzing the morphology of the Ln^{3+}−doped DNA DX lattices using atomic force microscopy (AFM). The interactions between Ln^{3+} and SDNA were examined using spectroscopic methods of UV–visible, Raman, and X-ray photoelectron spectroscopy (XPS). The current response with an external voltage applied to Ln^{3+}−doped SDNA thin films under UV exposure with different illumination powers was examined. Periodic photovoltage generation and rise- and fall-time analysis of Ln^{3+}-doped SDNA thin films under pulsed UV light at different light intensities were obtained and discussed in detail. Finally, we explained the charge transport mechanism in Ln^{3+}−doped SDNA thin films during UV illumination and analyzed the device stability in terms of photovoltage responsivity and retention properties.

2. Materials and methods

2.1. Materials and methods

For construction of Ln^{3+}-doped DNA DX lattices, high performance liquid chromatography purified synthetic oligonucleotides were purchased from Bioneer (Daejeon, Korea). The complexes were formed by mixing stoichiometric quantities of 8 individual DX strands, the appropriate amounts of $Er(NO_3)_3{\cdot}5H_2O$ and $Nd(NO_3)_3{\cdot}6H_2O$ (Sigma Aldrich), and a freshly cleaved mica substrate (size of 5.0 × 5.0 mm^2, Ted Pella, CA, USA) in 1 × TAE/Mg^{2+} (40 mM Tris base, 20 mM acetic acid, 1 mM EDTA (pH 8.0), and 12.5 mM magnesium acetate) buffer solution. The final concentration of DNA DX tiles ([DX]) was 50 nM by varying [Ln^{3+}] (*e.g.*, [Nd^{3+}] of 0.5 mM, [Er^{3+}] of 1.0 mM, and [Nd^{3+} and Er^{3+}] of 0.75 mM each) in a fixed volume of 250 μL. The mixture was then kept in a Styrofoam box with 2 L of boiled water and was allowed to cool from 95 to 25 °C for 24 h to enable the hybridization process. During annealing, the DX strands formed DX tiles (containing Ln^{3+}) in solution, followed by growth of polycrystalline Ln^{3+}-doped DX lattices on mica through substrate-assisted growth method. Finally,

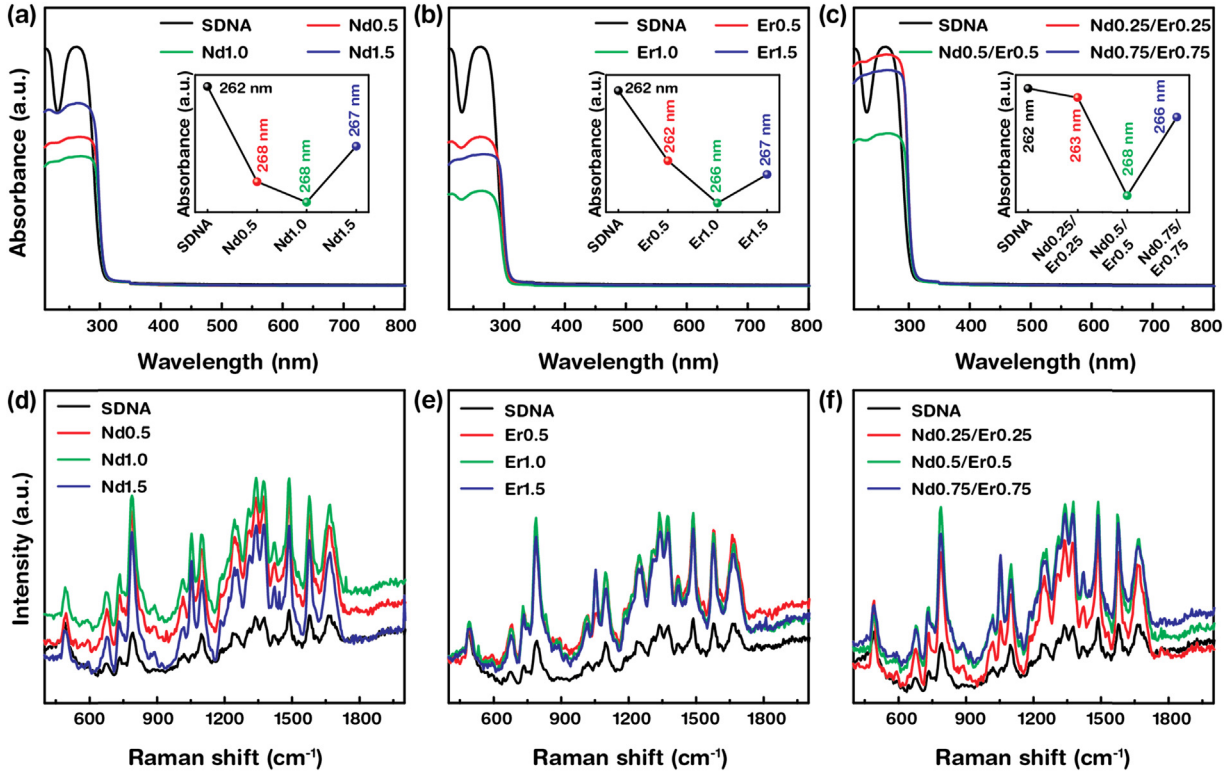

Fig. 2. UV–Visible absorption and Raman spectra of pristine SDNA and Ln^{3+}-doped SDNA thin films. (a, b) UV–Visible spectra of SDNA and Nd^{3+}- and Er^{3+}-doped SDNA thin films with different [Nd^{3+}] and [Er^{3+}] of 0.5, 1.0, and 1.5 mM. (c) UV–Visible spectra of Nd^{3+} and Er^{3+} co-doped SDNA thin films with [Nd^{3+}] and [Er^{3+}] of 0.25, 0.5, and 0.75 mM. The changes in absorption intensities and peak positions around the characteristic peak of DNA are shown in the insets. (d, e) Raman spectra of SDNA and Nd^{3+}- and Er^{3+}-doped SDNA thin films with different [Nd^{3+}] and [Er^{3+}]. (f) Raman spectra of Nd^{3+} and Er^{3+} co-doped SDNA thin films.

these polycrystalline Ln^{3+}-doped DX lattices fully covered the mica surface (Fig. 1, Fig. S1, Tables S1 and S2 in the Supporting information (SI)).

0.05 g of salmon DNA fibres (GEM Corporation, Shiga, Japan) and appropriate amounts of various [Ln^{3+}] (*e.g.*, [Nd^{3+}] of 1.0 mM, [Er^{3+}] of 1.5 mM, and [Nd^{3+} and Er^{3+}] of 0.5 mM each) were added to 10 mL of de-ionized (DI) water to obtain the Ln^{3+}—doped SDNA solution of 0.5 wt% (wt%). The mixture was stirred on a magnetic stirrer with a speed of 1000 RPM for 24 h at room temperature to obtain a uniformly dissolved solution. Finally, 20 μL of Ln^{3+}—doped SDNA solution was drop-casted onto an O_2 plasma-treated substrate (size of 5.0 × 5.0 mm^2; fused silica for UV–vis absorption, Raman, and XPS measurements and glass for current and photovoltage) and dried for 24 h to obtain a Ln^{3+}—doped SDNA thin film having a thickness of ~1.5 μm (Fig. 1).

2.2. Characterization techniques

An atomic force microscopy, UV–visible and Raman spectroscopes, and X-ray photoelectron spectroscopy were used to analyze the morphology, interactions, and binding modes of the Ln^{3+}—doped DNA thin films on a given substrate. The *I—V* and photovoltage characteristics were measured understand the transport and photoelectric effect under UV illumination (wavelength of 382 nm with varying input powers) as well as in the dark with a two-probe station connected to a lock-in amplifier containing an optical chopper. The detailed experimental conditions and instrumental information were mentioned in SI.

3. Results and discussion

3.1. Fabrication and topological analysis of Ln^{3+}-doped DNA thin films

Fabrication of the Ln^{3+}-doped DNA thin film and its utilization for photo detection under UV illumination are shown in Fig. 1. Fig. 1a displays a schematic of Ln^{3+} binding to a DNA phosphate group through electrostatic interaction and the DNA nitrogenous bases through intercalation. Ln^{3+}-doped DNA thin films were used for sensitive UV detection by measuring the generated photovoltage under UV illumination. Fig. 1b shows the experimental setup for photovoltage measurement *via* Ln^{3+}-doped DNA thin films.

Structural morphologies (crystalline or amorphous) of DNA DX lattices with varying concentrations of either single-doped (*i.e.*, Nd^{3+} or Er^{3+}) or co-doped Ln^{3+} (*i.e.*, Nd^{3+} and Er^{3+} mixed) were verified using AFM as shown in Fig. 1c-f and Fig. S2 in the SI. Up to a certain [Ln^{3+}], DNA DX lattices were formed without disturbing the lattice assembly during the course of annealing. We called this [Ln^{3+}] as the optimum concentration (*i.e.*, [Ln^{3+}]$_O$). From the observations, [Ln^{3+}]$_O$ (*i.e.*, either [Nd^{3+}]$_O$ or [Er^{3+}]$_O$) and [Nd^{3+}/Er^{3+}]$_O$ at a given DNA [DX] of 50 nM were found to be 1 mM for single-doping and 0.5 mM each for co-doping. Fig. S2 in the SI shows AFM images of DNA DX lattices having a [Nd^{3+}]$_O$ of 1.0 mM, a [Er^{3+}]$_O$ of 1.0 mM, and co-doped DNA DX lattices with [Nd^{3+}] and [Er^{3+}] of 0.5 mM each ([Nd^{3+}/Er^{3+}]$_O$), marked as Nd1.0, Er1.0, and Nd0.5/Er0.5, respectively. Periodicities and aperiodicities of the DNA DX tiles were verified using the fast Fourier transform (FFT) images obtained from the AFM images shown in the insets in Fig. 1 and Fig. S2 in the SI. From the FFT images, the unit building blocks (*i.e.*, DX tiles) with dimensions of 12.6 nm × 4.0 nm in the DNA DX lattice were clearly visible up to [Ln^{3+}]$_O$. In contrast, the DNA DX lattices were hardly visible above

$[Ln^{3+}]_O$ due to the geometrical constraints on the DNA duplexes induced from the excess of Ln^{3+}.

Even though DNA DX lattices with various $[Ln^{3+}]$ were used to find $[Ln^{3+}]_O$ by analyzing the morphological changes, physical properties (*e.g.*, UV–Visible spectrum, Raman, XPS, current, and photovoltage) were measured with Ln^{3+}-doped SDNA thin films because data acquisition with these films was more reliable than that of Ln^{3+}-doped DNA DX lattices. Naturally available SDNA molecules possess advantages such as easy fabrication, low cost, and mass production.

3.2. UV–visible and Raman spectroscopic analysis

UV–Visible spectroscopy was performed to understand the binding interaction of Ln^{3+} to the SDNA molecules. Fig. 2a-c illustrates the UV–Visible spectra of pristine, Ln^{3+}-doped, and co-doped SDNA thin films. Absorption intensities of Ln^{3+}-doped SDNA thin films around 260 nm decreased (*hypochromic*) with increasing $[Ln^{3+}]$ up to $[Ln^{3+}]_O$ due to the designated binding of Ln^{3+} to the SDNA, followed by the increase (*hyperchromic*) in intensities while increasing $[Ln^{3+}]$. Additionally, we observed the absorption peak shifts with various $[Ln^{3+}]$ as shown in insets in Fig. 2a-c. Interestingly, UV–Visible spectra of Nd^{3+} and Er^{3+} co-doped SDNA thin films exhibited similar trends as the single-doped films. The changes in absorption intensities around the characteristic peak of DNA occurred due to π- π interactions between the stacked base pairs and Ln^{3+} (Paston et al., 2017; Kesama et al., 2016).

Raman spectroscopy was performed as shown in Fig. 2d-f to understand the Ln^{3+} binding in the SDNA molecules. The spectra of single- and co-doped SDNA thin films with various $[Ln^{3+}]$ (*e.g.*, $[Nd^{3+}]$ of 1.5 mM for single-doping and $[Nd^{3+}]$ and $[Er^{3+}]$ of 0.25 mM each for co-doping) were obtained in the wavenumber range of 500–2000 cm^{-1}. The vibrational Raman peaks associated with DNA sugar, phosphate, and base groups possessing Ln^{3+} were identified. Significant enhancement of Raman peak intensities of Ln^{3+}-doped

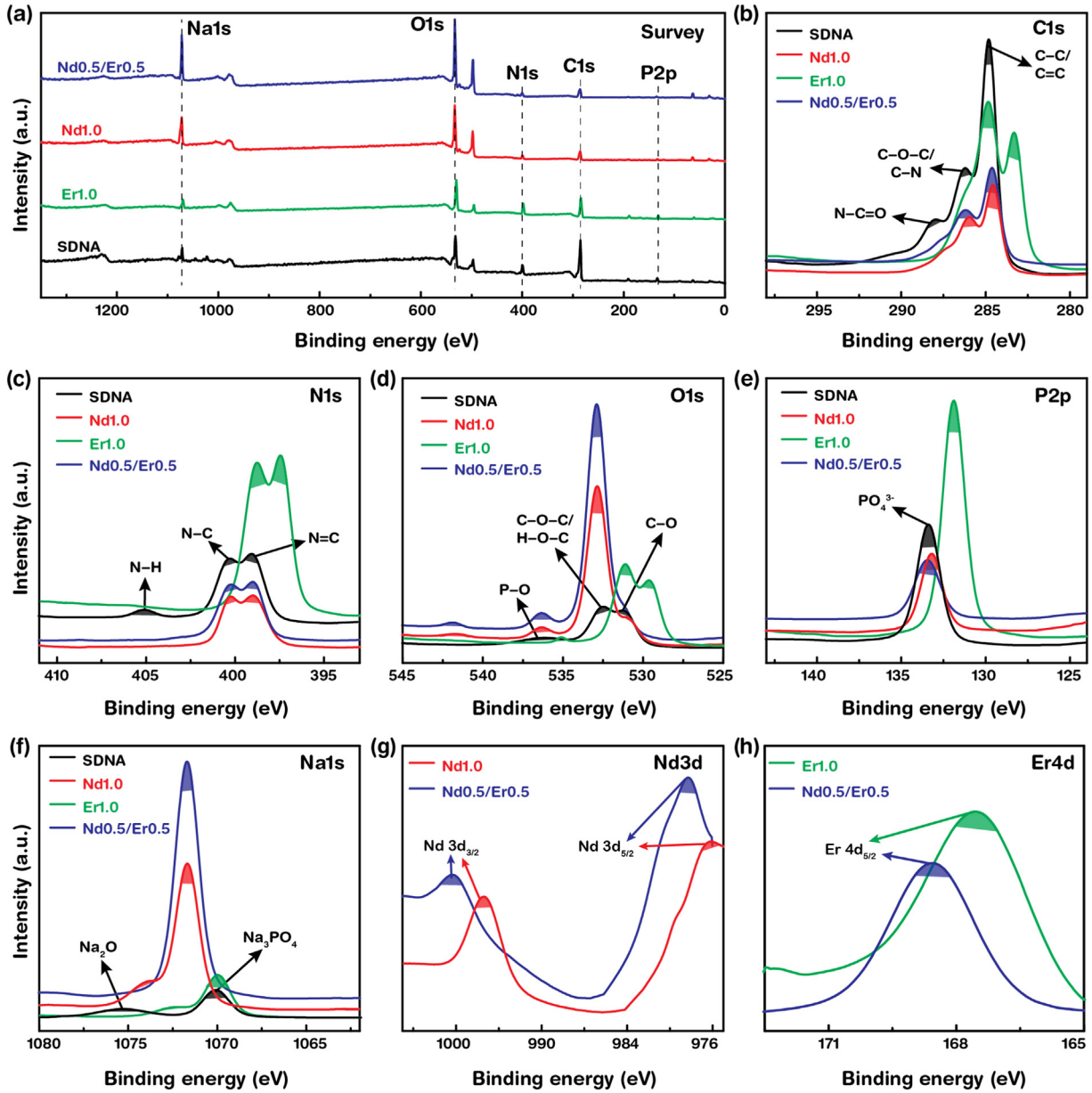

Fig. 3. X-ray photoelectron spectroscopy (XPS) survey and core spectra of SDNA thin films without and with Ln^{3+}. (a) Elemental survey spectra of SDNA and Ln^{3+}-doped SDNA thin films showing core elements. (b-f) Core spectra of C1s, N1s, O1s, P2p, and Na1s observed from the SDNA thin films. (g-h) Spin-orbit splitting peaks of 3d electron binding energies for Nd^{3+} ($3d_{3/2}$ and $3d_{5/2}$) and 4d electron binding energy for Er^{3+}($4d_{5/2}$).

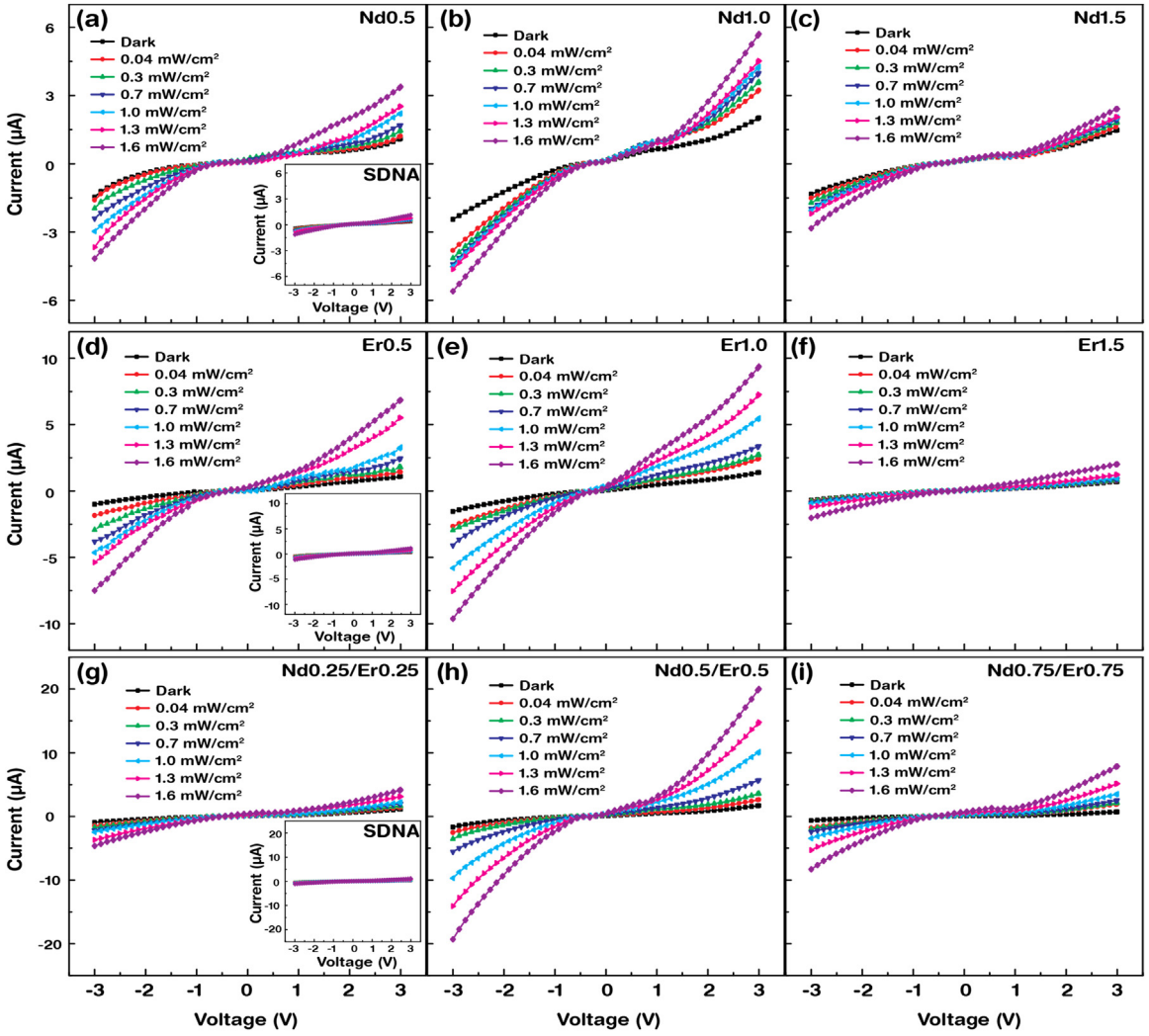

Fig. 4. Electrical measurement of pristine SDNA and Ln^{3+}-doped SDNA thin films under UV illumination with varying power intensities. (a-f) Current curves of SDNA (shown in insets) and Nd^{3+}- and Er^{3+}-doped SDNA thin films with different [Nd^{3+}] and [Er^{3+}] under UV illumination. (g-i) Current curves of SDNA and Nd^{3+} and Er^{3+} co-doped SDNA thin films under UV illumination with different power intensities.

SDNA thin films compared to pristine SDNA were observed, especially in the sugar-phosphate regions at 788, 1053, 1099, 1236 cm^{-1} and nitrogenous base regions at 1336, 1376, 1487, and 1664 cm^{-1} (Muntean et al., 2005; Kang et al., 2016). Interestingly, maximum intensities of the peaks occurred at single-doped SDNA thin films with a [Nd^{3+}] of 1.0 mM, a [Er^{3+}] of 1.0 mM, and co-doped SDNA thin films with [Nd^{3+}] and [Er^{3+}] of 0.5 mM each, which corresponded to [Nd^{3+}]$_O$, [Er^{3+}]$_O$, and [Nd^{3+}/Er^{3+}]$_O$ observed from the AFM topological analysis.

3.3. XPS analysis

Fig. 3 displayed the XPS survey and core spectra (*i.e.*, C1s, N1s, O1s, P2p, and Na1s) of SDNA thin films without and with [Ln^{3+}]$_O$. Here, XPS was used to analyze the elemental composition and chemical bonding of the formed Ln^{3+}-doped SDNA complexes. By comparing the core element spectra of the Ln^{3+}-doped SDNA thin films with the SDNA, the binding energy shift and peak intensity change were observed, which indicated the presence of Ln^{3+} in SDNA. From N1s core spectra in pristine SDNA, the peaks at 405, 400, and 399 eV corresponded to the chemical bonding of N-H, N-C, and N = C, respectively. The N-H peak in pristine SDNA disappeared upon Ln^{3+} doping. In addition, Nd^{3+}- and Nd^{3+}/Er^{3+}-doped SDNA thin films showed suppressed intensities, while Er^{3+}-doped SDNA revealed noticeable negative shift in binding energies at N-C and N = C (Fig. 3c) (Barber and Clark, 1970). Similar trends were observed with the P2p spectra (Fig. 3e). These behavior signified that the Ln^{3+} were bound between the bases (*via* chemical intercalations) and to the phosphate backbone of DNA (*via* electrostatic interactions). In the XPS core spectra of Nd3d and Er4d, significant positive peak shifts (*i.e.*, binding energy of Nd $3d_{5/2}$ from 976.28 to 978.28 eV; Nd $3d_{3/2}$ peak from 997.38 to 1000.33 eV; and $Er4d_{5/2}$ peak from 167.58 to 168.58 eV) were observed with intensity changes for Nd^{3+} and Er^{3+} co-doped SDNA thin films compared to the single-doped SDNA (Fig. 3g,h). These results verified that the Ln^{3+} was doped in the SDNA duplexes (Dinsmore and Lee, 2008; Petrovykh et al., 2004; Petrovykh et al., 2003).

3.4. Current (I)-voltage (V) measurements in dark and under UV illuminations

Electrical measurements for SDNA and Ln^{3+}-doped SDNA thin films in the dark (dark current observed, I_d) and under UV illumination (photocurrent observed under UV, I_p) with varying power intensities were conducted (Fig. 4). The I_d of Ln^{3+}-doped SDNA thin films measured in the dark was up to ~7 times higher than that of pristine SDNA due to the reduction of energy band gap while doping (Dugasani et al., 2014a, 2014b). Under UV illumination, the I_p of Ln^{3+}-doped SDNA thin films increased drastically, especially at a [Nd^{3+}]$_O$ of 1.0 mM, a

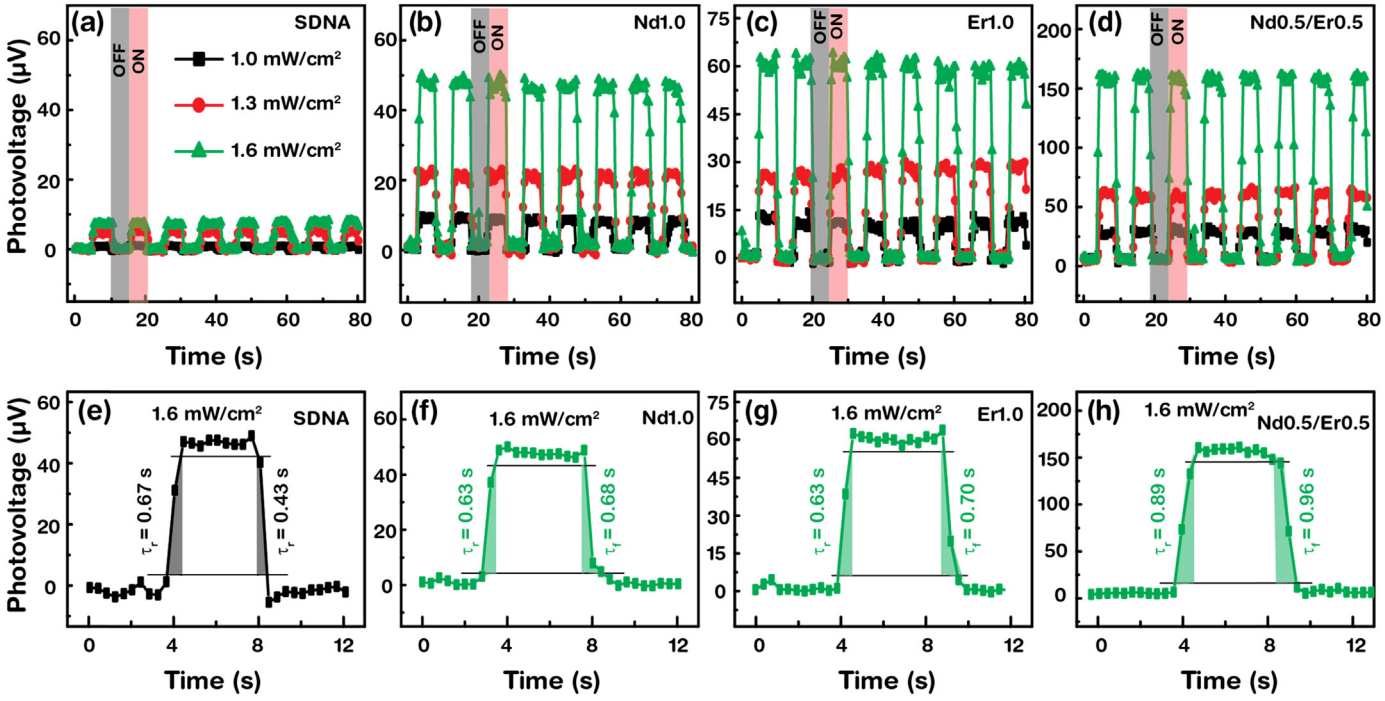

Fig. 5. Cyclic photovoltage responses and rise-time (τ_r) and fall-time (τ_f) analysis of pristine SDNA and Ln^{3+}-doped SDNA thin films under UV light. (a-d) Time-dependent photovoltage response curves of pristine SDNA and Ln^{3+}-doped SDNA thin films (*i.e.,* Nd1.0, Er1.0, and Nd0.5/Er0.5) measured under UV light at three different light intensities *i.e.*,1.0, 1.3, and 1.6 mW/cm^2. (e-h) τ_r and τ_f comparisons of pristine SDNA and Ln^{3+}-doped SDNA thin films obtained at 1.6 mW/cm^2.

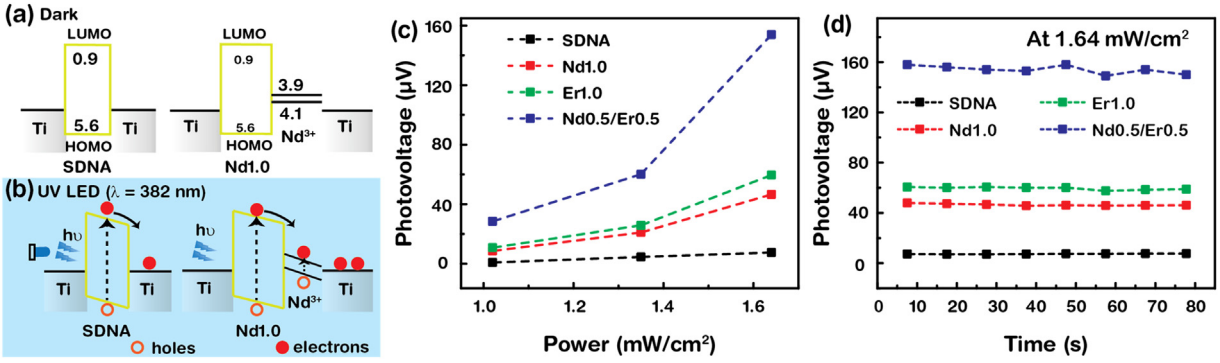

Fig. 6. Energy band representation and photovoltages as a function of power and time of pristine SDNA and Ln^{3+}-doped SDNA photodetectors. (a, b) Energy band diagrams of SDNA and Nd^{3+}-doped SDNA in the dark (flat HOMO and LUMO levels) and under UV illumination (flow of electrons from HOMO and LUMO causes a tilt in the band). (c) Photovoltage responsivities of Ln^{3+}-doped SDNA thin films with respect to the illuminated light intensity. (d) Photovoltages of Ln^{3+}-doped SDNA thin films as a function of time for device stability.

$[Er^{3+}]_O$ of 1.0 mM, and for co-doped SDNA thin films with a $[Nd^{3+}/Er^{3+}]_O$ of 0.5 mM. This might be because the maximum portion of the available binding sites of Ln^{3+} (which interacted with the UV light to enhance I_p) in SDNA were achieved without geometrical changes in the duplexes (Dugasani et al., 2015a, 2015b, 2015c). Above $[Ln^{3+}]_O$, the I_p decreased since non-specific binding of the Ln^{3+} to the SDNA occurred in the presence of excess Ln^{3+}. Interestingly, the I_p of the co-doped SDNA thin films with $[Nd^{3+}/Er^{3+}]_O$ at 3 V was 2–3 magnitudes higher than the single-doped SDNA with either $[Er^{3+}]_O$ or $[Nd^{3+}]_O$ because of the relatively better arrangement of mixed Nd^{3+} and Er^{3+} in SDNA (Fig. 4b, e, h).

3.5. Photovoltage and rise-time (τ_r) and fall-time (τ_f) analysis

Photovoltage responses and rise-time (τ_r) and fall-time (τ_f) analysis of pristine SDNA and Ln^{3+}-doped SDNA thin films under UV light at varying light intensities (*i.e.*, 1.0, 1.3, and 1.6 mW/cm^2) are displayed in Fig. 5. The photovoltages were monotonically enhanced with increasing light illumination power (as expected) due to the increased charge carrier density. The simplified experimental setup of the ON/OFF UV light switching for Ln^{3+}-doped SDNA thin films is shown in Fig. 1. For single- and co-doped SDNA thin films, we observed a considerable increase in photovoltage responses (*i.e.*, 5-fold increase for Nd^{3+}, 10-fold for Er^{3+}, and 13-fold for Nd^{3+}/Er^{3+}) compared to the pristine SDNA. In addition, stability of the photovoltage generation and sensitivity of the photodetection, which are crucial for various functionalized optoelectronic devices, were explained by analyzing the magnitude of the photovoltage response and by calculating the τ_r and τ_f response times, respectively. We observed no noticeable decrease in the photovoltages of single- and co-doped SDNA thin films up to 8 illumination cycles, which indicated that the photodetectors were highly stable, robust, and durable with respect to time. We obtained the stability curves of the Ln^{3+}-doped SDNA thin films which were displayed in Fig. S3 in SI. Photovoltage response of Ln^{3+}-doped SDNA thin films under continuous UV light illumination for 800 s revealed that there was no noticeable degradation and deterioration in the performance.

The τ_r (τ_f) was defined as the time from 10% to 90% (90–10%) of the maximum photovoltage peak value after switching ON (OFF) the UV illumination. Interestingly, we noticed clear differences of τ_r and τ_f ($\Delta\tau_r \leq 0.2$ s and $\Delta\tau_f \leq 0.5$ s) between pristine SDNA (having relatively lower photovoltage peak values than Ln^{3+}-doped) and Ln^{3+}-doped SDNA (having extra charge carriers) thin films than the previous report (Sanchez et al., 2013).

3.6. Energy band diagram representations and photoresponses

The possible energy band diagram explains the enhancement of the photovoltage peak values of Ln^{3+}-doped SDNA thin films compared to pristine SDNA under UV illumination (Fig. 6a,b). The highest occupied molecular orbital (HOMO) and lowest un-occupied molecular orbital (LUMO) energy bands were flat in the dark as shown in Fig. 6a. In contrast, the electrons excited from the HOMO to the LUMO energy bands in SDNA thin films caused a tilt in the band under UV illumination, which was responsible for a noticeable enhancement in the photovoltages (Fig. 6b, left) (Schinzel et al., 2006). In the Ln^{3+}—doped SDNA thin films (Fig. 6b, right), a flow of electrons from HOMO to LUMO energy bands was generated in both SDNA and Ln^{3+} under illumination resulting in accumulation of more charges. Therefore, the excess charge carriers generated in both SDNA and Ln^{3+} are attributed to the significant enhancement of the photovoltage peak values.

Measured photovoltage peak values of SDNA and Nd^{3+}-, Er^{3+}-, and Nd^{3+}/Er^{3+}-doped SDNA thin films as a function of UV light power intensity and UV exposure time are displayed in Fig. 6c,d. The instantaneous responsivities, which are defined as the photovoltage divided by power at 1.64 mW/cm^2, were 4.6, 28.4, 36.3, and 94.1 μV·cm^2/mW for the pristine SDNA and Nd^{3+}-, Er^{3+}-, and Nd^{3+}/Er^{3+}-doped SDNA thin films, respectively. These results indicated significant enhancement in photovoltage responsivities through additional charge carriers in SDNA thin films by single-doping (up to ~10 times) and co-doping (up to ~30 times). The photovoltages for pristine SDNA and Nd^{3+}-, Er^{3+}-, and Nd^{3+}/Er^{3+}-doped SDNA thin films at 1.64 mW/cm^2 for 80 s were collected, and no noticeable degradation in performance was observed, as portrayed in Fig. 6d. Another important parameter for photodetectors is the on/off ratio. The on/off ratio is defined as the ratio of photovoltage under illumination to the photovoltage obtained under dark. The on/off ratios of Nd1.0, Er1.0, and Nd0.5/Er0.5 were 120, 125, and 317, respectively (obtained at a power intensity of 1.6 mW/cm^2 which was relatively lower power intensity than the previously reported photodetectors (Table S3 in SI)). Thus, the photodetecting devices made of Ln^{3+}-doped SDNA thin films were very stable and showed endurable performance.

4. Conclusions

DNA DX lattices and naturally available SDNA thin films with single-doped Nd^{3+} or Er^{3+} and co-doped Nd^{3+}/Er^{3+} were fabricated by controlling the concentration of Ln^{3+} relative to the DNA molecules for high performance UV detection. The optimum concentrations of Ln^{3+} were estimated to be 1.0 mM for Nd^{3+}, 1.0 mM for Er^{3+}, and 0.5 mM each for Nd^{3+}/Er^{3+} by analyzing the morphology of the single- and co-doped DNA DX lattices using AFM. We performed UV–Visible spectroscopy to understand the binding interaction of the Ln^{3+} to the SDNA molecules by monitoring the changes in absorption intensities and peak shifts at ~260 nm. Raman spectroscopy was performed to understand the Ln^{3+} binding in the SDNA molecules. Significant changes in the vibrational Raman peak intensities associated with DNA sugar, phosphate, and base groups possessing Ln^{3+} were observed. The elemental composition and chemical bonding of the formed Ln^{3+}-doped SDNA complexes were confirmed by XPS. Electrical measurements for Ln^{3+}-doped SDNA thin films under UV illumination with varying power intensities were conducted. The photocurrent of Ln^{3+}-doped SDNA thin films at $[Ln^{3+}]_O$ increased significantly under UV illumination. This might be because a relatively larger portion of available binding sites of Ln^{3+} in SDNA was present. Cyclic photovoltage response and photovoltage rise- and fall-time analysis of Ln^{3+}-doped SDNA thin films under UV illumination were measured. We observed considerable increases in photovoltage responses, *i.e.*, a 5-fold increase for Nd^{3+}, 10-fold for Er^{3+}, and 13-fold for Nd^{3+}/Er^{3+}, compared to the pristine SDNA. Performance of the photodetectors made of DNA was measured in photovoltage responsivity and retention properties, which indicated the high stability and substantial endurance of Ln^{3+}-doped SDNA thin films. Hence, we can construct sensitive and efficient photodetectors by using specific function-embedded DNA thin films with an easy and simple fabrication procedure.

Acknowledgements

This research was supported by the National Research Foundation of Korea (NRF) (2017R1E1A1A01073076, 2016R1D1A1B03933768, 2017R1A2B4010955, and 2018R1A2B6008094).

Appendix A. Supplementary material

Supplementary data associated with this article can be found in the online version at doi:10.1016/j.bios.2018.10.042.

References

Barber, M., Clark, D.T., 1970. J. Chem. Soc. D 24–25.
Dinsmore, M.J.J.S., Lee, M.J., 2008. J. Inorg. Biochem. 102, 1599–1606.
Dugasani, S.R., Lee, N., Lee, J., Kim, B., Hwang, S.U., Lee, K.W., Kang, W.N., Park, S.H., 2013. Sci. Rep. 3, 1819.
Dugasani, S.R., Ha, T., Gnapareddy, B., Choi, K., Lee, J., Kim, B., Kim, J.H., Park, S.H., 2014a. ACS Appl. Mater. Interfaces 6, 17599–17605.
Dugasani, S.R., Kim, J.A., Kim, B., Joshirao, P., Gnapareddy, B., Vyas, C., Kim, T., Park, S.H., Manchanda, V., 2014b. ACS Appl. Mater. Interfaces 6, 2974–2979.
Dugasani, S.R., Kim, M., Lee, I.Y., Kim, J.A., Gnapareddy, B., Lee, K.W., Kim, T., Huh, N., Kim, G.-H., Park, S.C., Park, S.H., 2015a. Nanotechnology 26, 275604.
Dugasani, S.R., Lee, K.W., Kim, S.J., Yoo, S., Gnapareddy, B., Jung, J., Jung, T.S., Bashar, S., Kim, H.J., Park, S.H., 2015b. Appl. Phys. Lett. 106, 263702.
Dugasani, S.R., Park, B., Gnapareddy, B., Pamanji, S.R., Yoo, S., Lee, K.W., Lee, S., Jun, S.C., Kim, J.H., Kim, C., Park, S.H., 2015c. RSC Adv. 5, 55839–55846.
Gong, X., Tong, M., Xia, Y., Cai, W., Moon, J.S., Cao, Y., Yu, G., Shieh, C.L., Nilsson, B., Heeger, A.J., 2009. Science 325, 1665–1667.
Halley, P.D., Lucas, C.R., McWilliams, E.M., Webber, M.J., Patton, R.A., Kural, C., Lucas, D.M., Byrd, J.C., Castro, C.E., 2016. Small 12, 308–320.
Jung, J., Kim, S.J., Yoon, D.H., Kim, B., Park, S.H., Kim, H.J., 2012. ACS Appl. Mater. Interfaces 5, 98–102.
Kang, D.H., Dugasani, S.R., Park, H.Y., Shim, J., Gnapareddy, B., Jeon, J., Lee, S., Roh, Y., Park, S.H., Park, J.H., 2016. Sci. Rep. 6, 20333.
Kesama, M.R., Dugasani, S.R., Yoo, S., Chopade, P., Gnapareddy, B., Park, S.H., 2016. ACS Appl. Mater. Interfaces 8, 14109–14117.
Khokhra, R., Bharti, B., Lee, H.N., Kumar, R., 2017. Sci. Rep. 7, 15032.
Kim, H.U., Dugasani, S.R., Kulkarni, A., Gnapareddy, B., Kim, J.A., Park, S.H., Kim, T., 2015. RSC Adv. 5, 67712–67717.
Lee, K.W., Kim, K.M., Lee, J., Amin, R., Kim, B., Park, S.K., Lee, S.K., Park, S.H., Kim, H.J., 2011. Nanotechnology 22, 375202.
Mitta, S.B., Dugasani, S.R., Jung, S.-G., Vellampatti, S., Park, T., Park, S.H., 2017. Nanotechnology 28, 405703.
Muntean, C.M., Dostál, L., Misselwitz, R., Welfle, H., 2005. J. Raman Spectrosc. 36, 1047–1051.
Nummelin, S., Kommeri, J., Kostiainen, M.A., Linko, V., 2018. Adv. Mater. 30, 1703721.
Osinsky, A., Gangopadhyay, S., Gaska, R., Williams, B., Khan, M.A., Kuksenkov, D., Temkin, H., 1997. Appl. Phys. Lett. 71, 2334–2336.
Paston, S.V., Polyanichko, A.M., Shulenina, O.V., 2017. J. Struct. Chem. 58, 399–405.
Pei, H., Liang, L., Yao, G., Li, J., Huang, Q., Fan, C., 2012. Angew. Chem. Int. Ed. 51, 9020–9024.
Petrovykh, D.Y., Suda, H.K., Whitman, L.J., Tarlov, M.J., 2003. J. Am. Chem. Soc. 125, 5219–5226.
Petrovykh, D.Y., Suda, H.K., Tarlov, M.J., Whitman, L.J., 2004. Langmuir 20, 429–440.
Rakitin, A., Aich, P., Papadopoulos, C., Kobzar, Y., Vedeneev, A.S., Lee, J.S., Xu, J.M., 2001. Phys. Rev. Lett. 86, 3670–3673.
Reisfeld, R., 1987. Inorg. Chim. Acta 140, 345–350.
Sanchez, L., Lembke, D., Kayci, M., Radenovic, A., Kis, A., 2013. Nat. Nanotechnol. 8, 497–501.
Schinzel, S., Bindl, M., Visseaux, M., Chermette, H., 2006. J. Phys. Chem. A. 110, 11324–11331.
Seeman, N.C., 2003. Nature 421, 427–431.
Song, X., Chang, M.H., Pecht, M., 2013. JOM 65, 1276–1282.
Vellampatti, S., Heo, R., Mitta, S.B., Park, J.H., Park, S.H., 2018. Nanotechnology. 29, 095602.
Vellampatti, S., Mitta, S.B., Kim, J.A., Hwang, T., Dugasani, S.R., Kim, T., Park, S.H., 2015. Curr. Appl. Phys. 15, 851–856.
Winfree, E., Liu, F., Wenzler, L.A., Seeman, N.C., 1998. Nature 394, 539–544.
Yoon, M., Min, S.W., Dugasani, S.R., Lee, Y.U., Oh, M.S., Anthopoulos, T.D., Park, S.H., Im, S., 2017. Small 13, 1703006.